



## Electrochemical properties of nanosize Sn-coated graphite anodes in lithium-ion cells

G.X. WANG\*, JANE YAO, JUNG-HO AHN, H.K. LIU and S.X. DOU

Battery Technology Research Program, Institute for Superconducting & Electronic Materials, University of Wollongong, NSW 2522, Australia

(\*author for correspondence, fax: +161-2-42215731, e-mail: gwang@uow.edu.au)

Received 28 March 2003; accepted in revised form 25 July 2003

**Key words:** lithium intercalation, lithium-ion battery, micro-encapsulation, Sn-coated graphite

### Abstract

A series of Sn-coated graphite composite materials for lithium-ion batteries were prepared by microencapsulating nanosize Sn particles in graphite. The nanosize Sn particles are homogeneously dispersed in the graphite matrix *via* electroless chemical reduction. The tin-graphite composite showed a great improvement in lithium storage capacity. Since Sn is an active element to lithium, Sn can react with lithium to form  $\text{Li}_{4.4}\text{Sn}$  alloys, a reaction accompanied by a dramatic volume increase, whereas the ductile graphite matrix provides a perfect buffer layer to absorb this volume expansion. Therefore, the integrity of the composite electrode is preserved during lithium insertion and extraction. Cyclic voltammetry was employed to identify the reaction process involved in lithium insertion and extraction in the graphite structure, as well as lithium alloying with tin. The tin-graphite composites provide a new type of anode material for lithium-ion batteries with an increased capacity.

### 1. Introduction

Lithium-ion batteries are the most advanced power sources for modern portable electronic devices and have demonstrated the highest energy density of all rechargeable batteries. Large-scale lithium-ion batteries have shown promise for use in electric vehicles (EVs). The energy density of lithium-ion batteries is determined by the lithium storage capacity of the cathode and anode materials. Carbonaceous materials and lithium cobalt oxides are currently used as anode and cathode materials in commercial lithium-ion batteries [1–4]. Carbon can react with lithium to form  $\text{LiC}_6$ , with a theoretical capacity of  $372 \text{ mAh g}^{-1}$ . In practice, a carbon anode gives a reversible capacity of  $300\text{--}320 \text{ mAh g}^{-1}$  [5, 6].

Recently, some new anode materials, including intermetallic alloys, tin oxide glass and lithium alloys, have received worldwide attention. In particular, tin has been employed as the active element, since it can combine with lithium to form  $\text{Li}_{22}\text{Sn}_5$  alloys with a theoretical capacity of  $990 \text{ mAh g}^{-1}$  [7, 8]. However, when tin is used alone as an anode material, it rapidly loses capacity. This is because of the large volume change associated with the formation of Li–Sn alloys, which leads to anode disintegration. This situation can be improved by reducing the Sn particle size. Other workers have demonstrated that nanosize or amorphous tin-based anode materials show better cycling performance [9, 10].

The objective of the present investigation is to develop new graphite composite anode materials by combining

the high lithium storage element Sn and graphite to achieve stable cyclability. Nanosize Sn particles were encapsulated in a graphite matrix by using electroless deposition. Different percentages of Sn were added to the graphite host. The physical properties and electrochemical performance were systematically examined.

### 2. Experimental

#### 2.1. Synthesis of Sn-coated graphite

Synthetic graphite was used as received from Aldrich Chemicals. Tin encapsulation was carried out at  $55^\circ\text{C}$  from an alkaline bath containing  $\text{SnCl}_2$  in NaOH solution. The graphite powders were dispersed by mechanical stirring, followed by ultrasonic treatment. During this process, sodium hypophosphite and sodium citrate solutions were respectively added in as the reducing agent and the complexing agent [11, 12]. The  $\text{Sn}^{2+}$  ions were reduced to elemental Sn *in situ* in the graphite matrix. The amount of tin loading was altered by changing the concentration of the  $\text{SnCl}_2$  solution. After completion of the coating, the tin-graphite composites were thoroughly washed with de-ionised water and dried in a vacuum oven. The concentration of tin in the solution bath was analysed, and this was used to estimate the amount of Sn deposition. Three different composites were prepared with Sn contents of 10, 15 and 20% by weight.

## 2.2. Material characterisation

The particle size distribution was measured with a Malvern Particle Size Analyser. The morphology and surface compositions of the bare and tin-encapsulated graphite were analysed by scanning electron microscopy (SEM). The phase composition was characterised by X-ray diffraction (XRD) using a Philips PW 1730 diffractometer with Cu K $\alpha$  radiation.

## 2.3. Electrochemical measurement

Tin-graphite composite negative electrodes were made by dispersing 95 wt% active materials and 5 wt% polyvinylidene fluoride (PVDF) binder in dimethyl phthalate solvent to form a slurry. The slurry was then spread on to a copper foil, which was then cut into a  $\phi$ 12 mm disk. Teflon testing cells were assembled in an argon filled glove-box (MBraun, Unilab, USA). The electrolyte was 1 M LiPF<sub>6</sub> in a mixture of ethylene carbonate (EC) and dimethyl carbonate (DMC) (1:1 by volume, provided by MERCK KgaA, Germany). The cells were galvanostatically charged and discharged within the voltage range 0–1.5 V vs Li/Li<sup>+</sup>. Cyclic voltammograms (CVs) were measured at a scan rate of 0.01 mV s<sup>-1</sup> using an EG&G scanning potentiostat (Model 362).

## 3. Results and discussion

### 3.1. Physical characterisation of tin-graphite composites

The particle size distribution of the graphite powders is shown in Figure 1. The graphite powders have an average particle size of 10  $\mu$ m with a Gaussian particle size distribution. Figure 2 shows SEM images of the bare graphite and tin-graphite powders. The bare graphite shows a flake type crystal shape. Some small crystals are present together with much larger crystals. As shown in the SEM photograph, tin was chemically deposited on the graphite structure, which is indicated

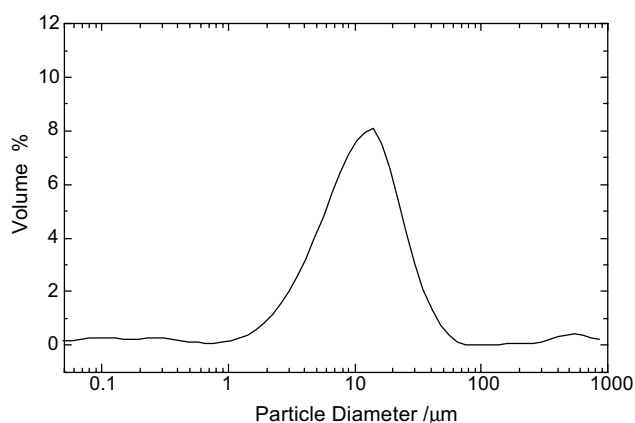


Fig. 1. Particle size distribution of the graphite powder.

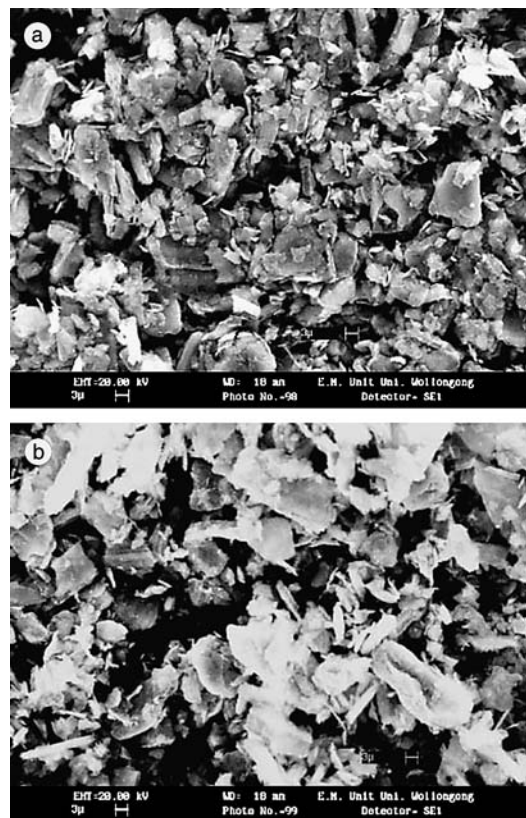


Fig. 2. SEM image of (a) bare graphite powder, (b) 20 wt% Sn-graphite composite powder.

by bright spots on the surface of the graphite powder. Energy dispersive spectroscopy (EDS) analysis of the tin-graphite composites confirmed the presence of tin.

XRD was performed on the tin-graphite composites. Figure 3 shows the XRD patterns of the bare graphite, tin-coated graphite, and annealed tin-coated graphite. The graphite powders are a well-graphitised 2 H graphite with a strong (002) diffraction line. The  $d_{002}$  space of  $d_{002}$  equals 3.35 Å, which is the value of perfect graphite. The Sn diffraction lines do not appear on the XRD pattern of the Sn-coated graphite composite. This

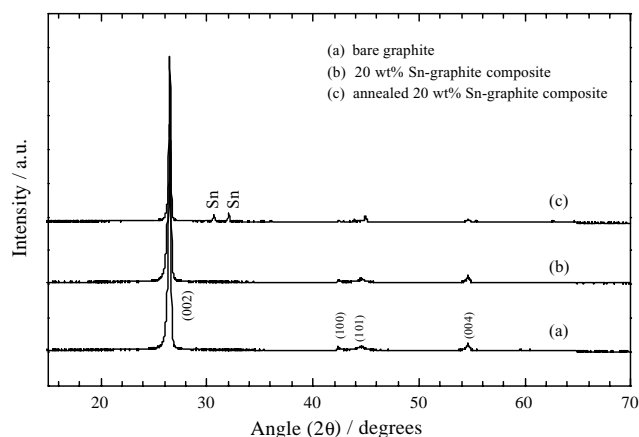


Fig. 3. The XRD patterns of (a) bare graphite, (b) 20 wt% Sn-graphite composites, (c) annealed 20 wt% Sn-graphite composite.

is because the chemically deposited Sn particles are nanosize in nature and cannot be detected by XRD. The Sn-coated graphite composites were then annealed at 300 °C in an argon atmosphere to re-crystallise the Sn particles. After annealing, the Sn diffraction lines appear on the XRD pattern (as shown in Figure 3c). This clearly indicates that Sn is added into the bulk of the graphite powders through electroless chemical deposition.

### 3.2. Electrochemical measurement of Sn-graphite composite electrodes

The electrochemical performance of Sn-graphite composites was measured using Sn-graphite as the working electrode and lithium metal as the counter electrode. Figure 4 shows the CVs of bare graphite and Sn-graphite composite electrodes. For the bare graphite electrode, one pair of redox reaction peaks are present on the CV curves. The potential of lithium insertion is close to 0.0 V vs the  $\text{Li/Li}^+$  reference electrode, whereas the potential for lithium extraction is around 0.2 V. As shown in Figure 4b and c, Sn-graphite electrodes show several reduction and oxidation peaks. These additional redox reaction peaks are related to the participation of elemental Sn. In the CV curves, the reduction peaks at 0.2 and 0.1 V are believed to originate from lithium alloying with Sn to form  $\text{Li}_x\text{Sn}$  alloy compounds. With increasing Sn content, the additional reaction peaks become more and more obvious. Cyclic voltammetry has identified the participation of Sn alloying with lithium. Further confirmation needs to be made by *in situ* XRD.

Figure 5 shows the discharge/charge profiles for bare graphite and Sn-graphite composite electrodes. The bare graphite electrode delivers a lithium insertion capacity of  $350 \text{ mAh g}^{-1}$  in the first lithiation process. When charging, about  $25 \text{ mAh g}^{-1}$  capacity was lost in the first cycle, which could have been consumed in the formation of the passivation film on the surface of the electrode. The 10 wt% Sn-graphite, 15 wt% Sn-graphite, and 20 wt% Sn-graphite electrodes demonstrated lithium insertion capacities of 495, 525 and  $590 \text{ mAh g}^{-1}$ , respectively, in the first discharge. These Sn encapsulated graphite composite electrodes have much higher lithium storage capacities than the bare graphite electrode. The extra lithium insertion capacity may be attributed to the presence of Sn in the graphite structure.

For all the electrodes, both the bare graphite and the Sn-graphite composites, the shape of the first discharge curve is different from that of the subsequent cycles. The major difference is that there is a smooth curve between 1.5 and 0.25 V in the first cycle for all the electrodes tested. This is not repeated in the subsequent cycles. It is well known that a passivation film or so-called solid electrolyte interface (SEI) forms in the initial lithium insertion process. This film is critical in stabilising the electrode for lithium insertion and extraction [13–15]. After the first cycle, the shape of the charge/discharge

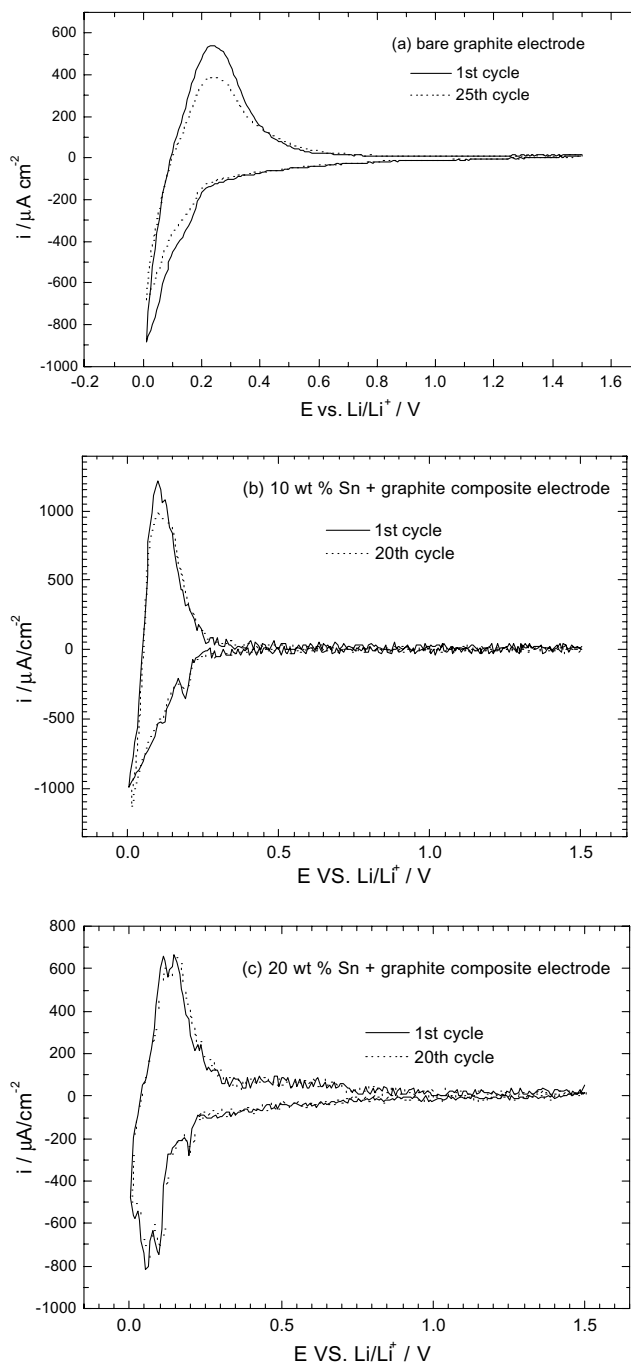


Fig. 4. CVs of (a) bare graphite, (b) 10 wt% Sn-graphite, (c) 20 wt% Sn-graphite.

curves remains almost invariant. This demonstrates that bare graphite and Sn-graphite composite electrodes are stable under repeated lithium intercalation and de-intercalation.

The cyclability of bare graphite and Sn-graphite electrodes is shown in Figure 6. The bare graphite electrode shows a stable capacity on cycling. All the Sn-graphite composite electrodes have an approximate  $3 \text{ mAh g}^{-1}$  rates of capacity decrease per cycle, which is higher than that of the bare graphite electrode. After the initial capacity drop in the first few cycles, the Sn-graphite composite electrode becomes stable. The

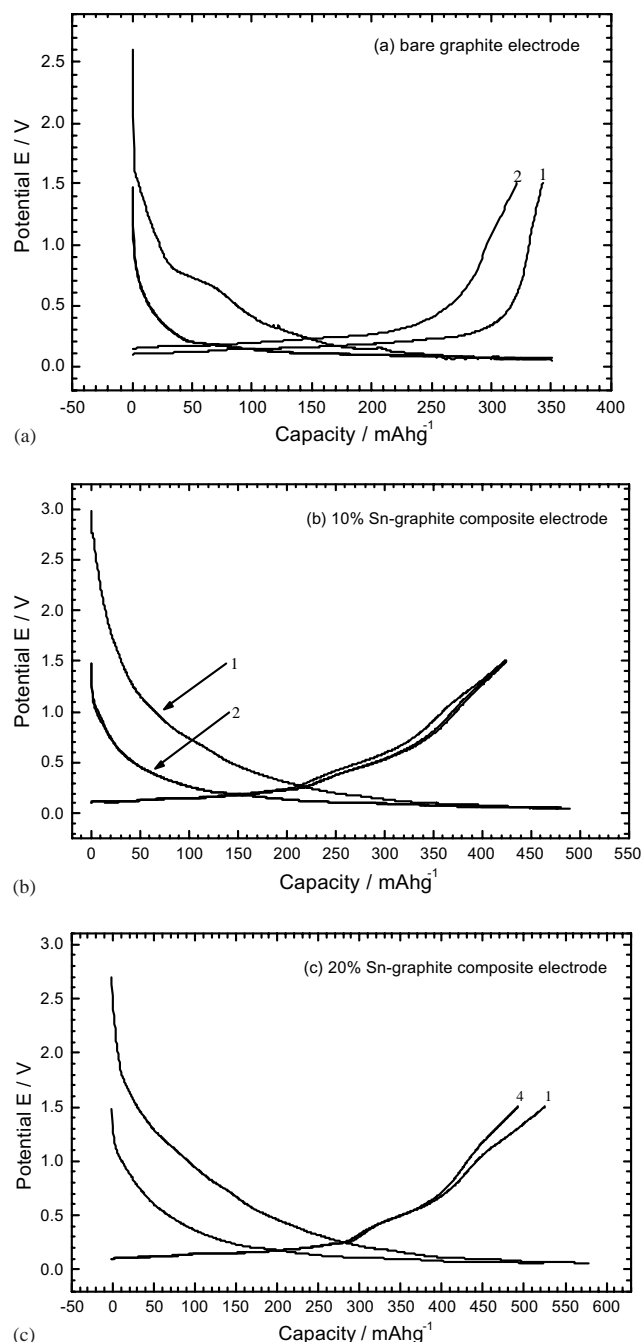


Fig. 5. The charge/discharge profiles of (a) bare graphite, (b) and (c) Sn-graphite composites.

chemically deposited Sn particles are nanosize in nature. When encapsulated in the graphite structure, the ductile graphite could act as a buffer layer to absorb the volume expansion of the resultant  $\text{Li}_x\text{Sn}$  alloy compounds. Therefore, the integrity of the electrode is preserved, which contributes to the stable cyclability of Sn-graphite composite electrodes. However, further improvements are required to increase the cycle life.

#### 4. Conclusions

Sn-graphite composites were prepared by electroless chemical deposition. EDS and XRD analysis confirmed

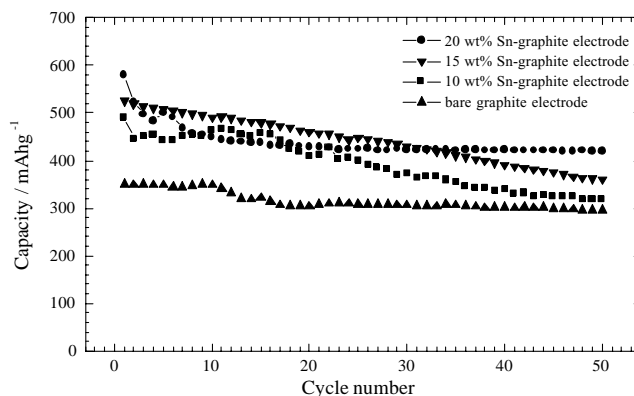


Fig. 6. The lithium intercalation capacity vs cycle number.

the presence of Sn in the graphite structure. Cyclic voltammetry showed extra reduction and oxidation peaks, which are related to the formation of  $\text{Li}_x\text{Sn}$  alloy compounds. Sn-graphite composite electrodes demonstrated a much higher lithium storage capacity than bare graphite. Due to the nature of the nanosized encapsulated Sn particles in the ductile graphite structure, Sn-graphite composite electrodes have shown relatively stable cyclability.

#### Acknowledgement

Financial support from the Australian Research Council (ARC) is gratefully acknowledged.

#### References

1. M.B. Armand, in D.W. Murphy, J. Broadhead and B.C. Steele (Eds), 'Material for Advanced Batteries' (Plenum Press, New York, 1980), p. 145.
2. D. Guymard and J.M. Tarascon, *J. Electrochem. Soc.* **139** (1992) 937.
3. J.B. Goodenough, A. Manthiram and B. Wnetrzewski, *J. Power Sources* **43/44** (1993) 269.
4. H. Katz, W. Bogel and J-P. Buchel, *J. Power Sources* **72** (1998) 43.
5. I. Kuribayashi, M. Yokoyama and M. Yamashita, *J. Power Sources* **54** (1995) 1.
6. T. Ohzuku, Y. Iwakoshi and K. Sawai, *J. Electrochem. Soc.* **140** (1993) 2490.
7. N. Takami, A. Satoh, M. Hara and T. Ohsaki, *J. Electrochem. Soc.* **142** (1995) 2564.
8. A. Claye and J.E. Fisher, *Electrochim. Acta* **45** (1999) 107.
9. Y. Idota, T. Kubota, A. Matsufuji, Y. Maekawa and T. Miyasaka, *Science* **276** (1997) 1395.
10. J.O. Bessenhard, J. Yang and M. Winter, *J. Power Sources* **68** (1997) 87.
11. B. Veeraraghavan, A. Durairajan, B. Haran, B. Popov and R. Guidotti, *J. Electrochem. Soc.* **149** (2002) A675.
12. P. Yu, J.A. Ritter, R.E. White and B.N. Popov, *J. Electrochem. Soc.* **147** (2000) 1280.
13. P. Liu and H. Wu, *J. Power Sources* **56** (1995) 81.
14. Y. Matsumura, S. Wang and J. Mondori, *J. Electrochem. Soc.* **142** (1995) 2914.
15. K.A. Hirasawa, T. Sato, H. Asahina, S. Yamaguchi and S. Mori, *J. Electrochem. Soc.* **144** (1997) L81.